AGU PUBLICATIONS

Geophysical Research Letters

RESEARCH LETTER
10.1002/2015GL064942

Key Points:
- Imaging of active faults beneath Long Beach, California
- New approach for seismic monitoring in a noisy environment
- Depth-dependent earthquake size distribution

Supporting Information:
- Text S1 and Figures S1–S4

Correspondence to:
A. Inbal,
ainbal@gps.caltech.edu

Citation:
Inbal, A., R. W. Clayton, and J.-P. Ampuero (2015), Imaging widespread seismicity at midlower crustal depths beneath Long Beach, CA, with a dense seismic array: Evidence for a depth-dependent earthquake size distribution, *Geophys. Res. Lett.*, *42*, 6314–6323, doi:10.1002/2015GL064942.

Received 13 JUN 2015
Accepted 24 JUL 2015
Accepted article online 29 JUL 2015
Published online 13 AUG 2015

Imaging widespread seismicity at midlower crustal depths beneath Long Beach, CA, with a dense seismic array: Evidence for a depth-dependent earthquake size distribution

Asaf Inbal[1], Robert W. Clayton[1], and Jean-Paul Ampuero[1]

[1] Seismological Laboratory, Division of Geological and Planetary Sciences, California Institute of Technology, Pasadena, California, USA

Abstract We use a dense seismic array composed of 5200 vertical geophones to monitor microseismicity in Long Beach, California. Poor signal-to-noise ratio due to anthropogenic activity is mitigated via downward-continuation of the recorded wavefield. The downward-continued data are continuously back projected to search for coherent arrivals from sources beneath the array, which reveals numerous, previously undetected events. The spatial distribution of seismicity is uncorrelated with the mapped fault traces, or with activity in the nearby oil-fields. Many events are located at depths larger than 20 km, well below the commonly accepted seismogenic depth for that area. The seismicity exhibits temporal clustering consistent with Omori's law, and its size distribution obeys the Gutenberg-Richter relation above 20 km but falls off exponentially at larger depths. The dense array allows detection of earthquakes two magnitude units smaller than the permanent seismic network in the area. Because the event size distribution above 20 km depth obeys a power law whose exponent is near one, this improvement yields a hundred-fold decrease in the time needed for effective characterization of seismicity in Long Beach.

1. Introduction

Monitoring microseismicity is the primary tool for illuminating active faults. This task is difficult in urban areas located near active plate boundaries, where the signal-to-noise ratio (SNR) is poor and the seismic hazard is high. One such example is the densely populated Los Angeles (LA) basin, a deep sedimentary basin traversed by several active faults, including the Newport-Inglewood Fault Zone (NIFZ), a major boundary fault in southern California. The NIFZ is well manifested by a series of small hills trending to the NW that extend for about 64 km between Culver City and Newport Beach (Figure 1). Since it bounds some of the region's most productive oil fields, the NIFZ has been drilled extensively, and this has revealed a complex fault geometry that consists of several overlapping en echelon strike-slip faults which cut through the oil bearing anticlines [*Barrows*, 1974; *Bryant*, 1988; *Wright*, 1991]. In Long Beach (LB), tectonic motion is primarily accommodated by a single strand known as the Cherry Hill Fault, which is a right-lateral strike-slip fault. It is subvertical down to about 5 km but may dip as much as 60° at larger depths [*Wright*, 1991]. Near its SE termination, the Cherry Hill Fault branches to the NW trending North East Flank Fault. The intersection is surficially expressed as a small uplifted wedge, known as Signal Hill, where most of the drilling activity in the LB Oil Field is currently taking place (Figure 1).

While reflection seismic surveys provide extensive data on the geometry of the NIFZ above 5 km, the structure of the NIFZ at larger depths is not well resolved, thus obtaining precise earthquake locations at those depths is important for hazard mitigation. The spatiotemporal distribution of microseismicity provides valuable information on the mechanics of fault slip and earthquake interactions and nucleation [*Rubin et al.*, 1999; *Rubin*, 2002; *Ziv*, 2006a; *Bouchon et al.*, 2011, 2013]. Activity in LB is not easily associated with the NIFZ and occurs primarily to the NE of the fault (Figure 1), with the largest recorded event being the 1933 M_w6.4 LB earthquake, located about 10 km SE of LB [*Hauksson and Gross*, 1991].

Efforts to monitor seismicity in the LA basin are hampered by poor SNR due to anthropogenic activity. Here we use a unique data set from a dense seismic array deployed in LB for exploration purposes (Figure 1) to search for events whose $M_w < 0$ and use their locations to resolve the fault geometry at depths larger than 5 km.

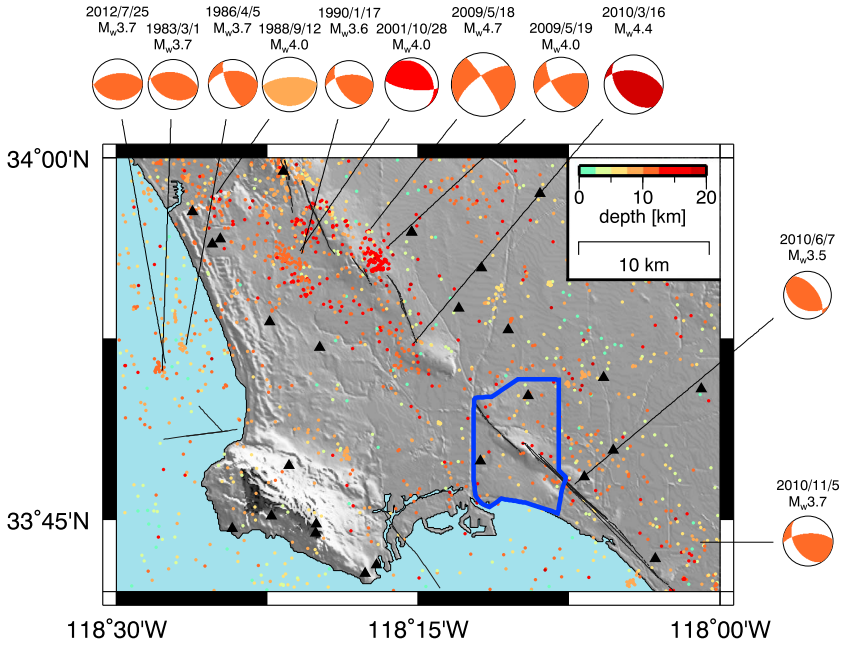

Figure 1. Location map and seismicity. Circles indicate relocated epicenters from *Hauksson et al.* [2012]. Focal mechanisms plotted for events with $M_w >= 3.5$ [*Yang et al.*, 2012]. Color indicates event depth. Black triangles and blue polygon are for the SCSN stations and LB array, respectively. Black curves are for the surface trace of mapped faults [*U.S. Geological Survey*, 2015].

2. Methods

We analyze continuous data from 5200 vertical 10 Hz geophones deployed in LB between January and June of 2011 [c.f. *Lin et al.*, 2013]. The array covers an area of 7 × 10 km, with an average sensor spacing of 110 m. Data were sampled 250 Hz and band-pass filtered at 5–10 Hz. Signals at frequencies above this range may be affected by spatial aliasing, while analyzing frequencies lower than 5 Hz significantly decreases our spatial resolution. We focus on the period between 1 March and 24 March, during which over 90% of the sensors were active. Recordings are contaminated by various anthropogenic noise sources, such as traffic from local freeways, landing at the LB airport, trains, and pumping in the LB Oil Field. The volume of our data set and the characteristics of anthropogenic signals in LB require that event detection be done automatically. Standard Short-Time-Average over Long-Time-Average (STA/LTA)-based detection algorithms are inadequate for our purposes, because such methods depend on the SNR of individual traces, and are thus easily distracted by spurious signals that originate from shallow noise sources in the vicinity of the geophones. Given the poor SNR, we turn to seismic array analysis to detect, locate, and determine the size of seismic events beneath LB. We only analyze nighttime data (6 P.M.–6 A.M.), because during these intervals noise levels in LB significantly decrease.

Our approach for event detection consists of two steps. In the first step we improve the SNR of the raw data by downward continuation, and in the second we continuously back project the downward-continued data to search for coherent high-frequency radiation from structures beneath the array. Downward continuation by phase-shift migration [*Claerbout*, 1976; *Gazdag*, 1978] is a common imaging technique used in geophysical exploration. We only analyze vertical component geophones and thus neglect *S* wave energy and use an approximate solution to the scalar (acoustic) wave equation. The acoustic wavefield on a surface, $p(x, y, z_0, t)$, is used as a boundary condition to determine $p(x, y, z_0 + \Delta z, t)$, the wavefield at depth $z = z_0 + \Delta z$. Assuming a depth-dependent, layered velocity model, the Fourier transformed data, $p(k_x, k_y, z_0, \omega)$, are downward continued to the target depth, z_n, with:

$$p\left(k_x, k_y, z_n, \omega\right) = p\left(k_x, k_y, z_0, \omega\right) \exp\left(-i \sum_{j=1}^{n} k_{z_j} h_j\right), \quad (1)$$

where k_x and k_y are the horizontal wave numbers, ω is the frequency, and h_j is the thickness of the j'th depth increment whose velocity is v_j. The vertical wave number, k_{z_j}, is equal to

$$k_{z_j} = \sqrt{\frac{\omega^2}{v_j^2} - \left(k_x^2 + k_y^2\right)}. \tag{2}$$

Imaginary values of k_{z_j} correspond to horizontally traveling evanescent waves. Their contributions to equation (1) are discarded in our analysis. The space-time domain representation of the downward continued wavefield is obtained by inverse Fourier transformation. In practice, data are downward continued to a depth of 5 km, for which the velocity model is well constrained from borehole data, and which is deep enough to suppress surface noise.

Downward continuation assumes the data are uniformly spaced and periodic. To avoid having wrapped-around signals contaminating the records, the traces and spatial domain are first zero-padded out to twice and 8 times the spatial and temporal dimensions of the data, respectively. Furthermore, in order to suppress the influence of strong spatial variations of SNR on the procedure, the data are first normalized by its hourly root-mean-square (RMS). We interpolate the data to a uniform grid whose cell size is 100×100 m, by assigning each data point a value equal to an exponentially weighted sum of its four nearest neighbors. Interpolation deamplifies phases with high incidence angles that are mostly generated by shallow sources. The amplitude difference between the raw and interpolated data can be as high as 10% inside the LB Oil Field, the noisiest area covered by the array, and is at a level of 3–5% in most other parts of the array. From synthetic tests presented in the supporting information, this procedure has a negligible effect on the location of events in the depth range of interest (Figure S2 in the supporting information). For a well-resolved wavefield, downward continuation significantly decreases the amplitude of uncorrelated noise relative to coherent signals with high apparent velocities, which are focused back to their origin point at depth. Given the slow seismic velocities beneath the array and the short interstation distances, wavefields with a characteristic frequency of up to about 15 Hz are well resolved by the LB array.

In the second step we back project the envelope of the downward-continued data to a volume beneath the array. By stacking the signal's envelope, we effectively reduce the sensitivity to unknown structure and focal mechanisms. The envelope, $s(t)$, is defined here by squaring the filtered, normalized, migrated waveforms, smoothing the squared waveforms using an 18-point (0.072 s) median window and decimating to a new sampling rate of 50 Hz.

The stacked envelope is defined as

$$S_i(t) = \frac{1}{n}\sum_{j=1}^{n} s(t + \tau_{ij}), \tag{3}$$

where n is the number of grid points on the downward-continuation target surface (same as the number of geophones) and τ_{ij} is the P wave traveltime difference between the j'th downward-continuation grid point and a reference grid point assuming a source located at the i'th backprojection grid point. When the source-receiver distance is much larger than the aperture of the array, the wavefront arriving at the array is typically approximated as a plane wave. However, given the LB array geometry and the distance to the sources we wish to image, this approximation is not valid. We therefore migrate the seismic envelopes and project the energy back to the origin. Theoretical traveltimes are computed on a mesh whose elements are 0.125 km^3 using a local 1-D velocity model extracted from the Southern California Earthquake Center Community Velocity Model—Harvard (CVM-H) [*Süss and Shaw*, 2003; *Plesch et al.*, 2011]. We analyze the amplitude of the migrated stack to identify coherent energy in the frequency band of interest. Figure 2 presents the raw and downward-continued waveforms, and spatial distribution of the log of the stack amplitude of an $M_w = 0.4$ event whose focal depth is 14 km. Note that the arrivals are only visible after the data are downward continued.

The detection is carried out by selecting the locations that correspond to the maximum power in the backprojection images, which are constructed from the peak amplitudes of nonoverlapping 5 s windows of the stacked envelopes. Because it is selected from images whose log amplitude is normally distributed (Figure S3), the noise in the maxima time series follows the Gumbel distribution, while the signal obeys a power law or

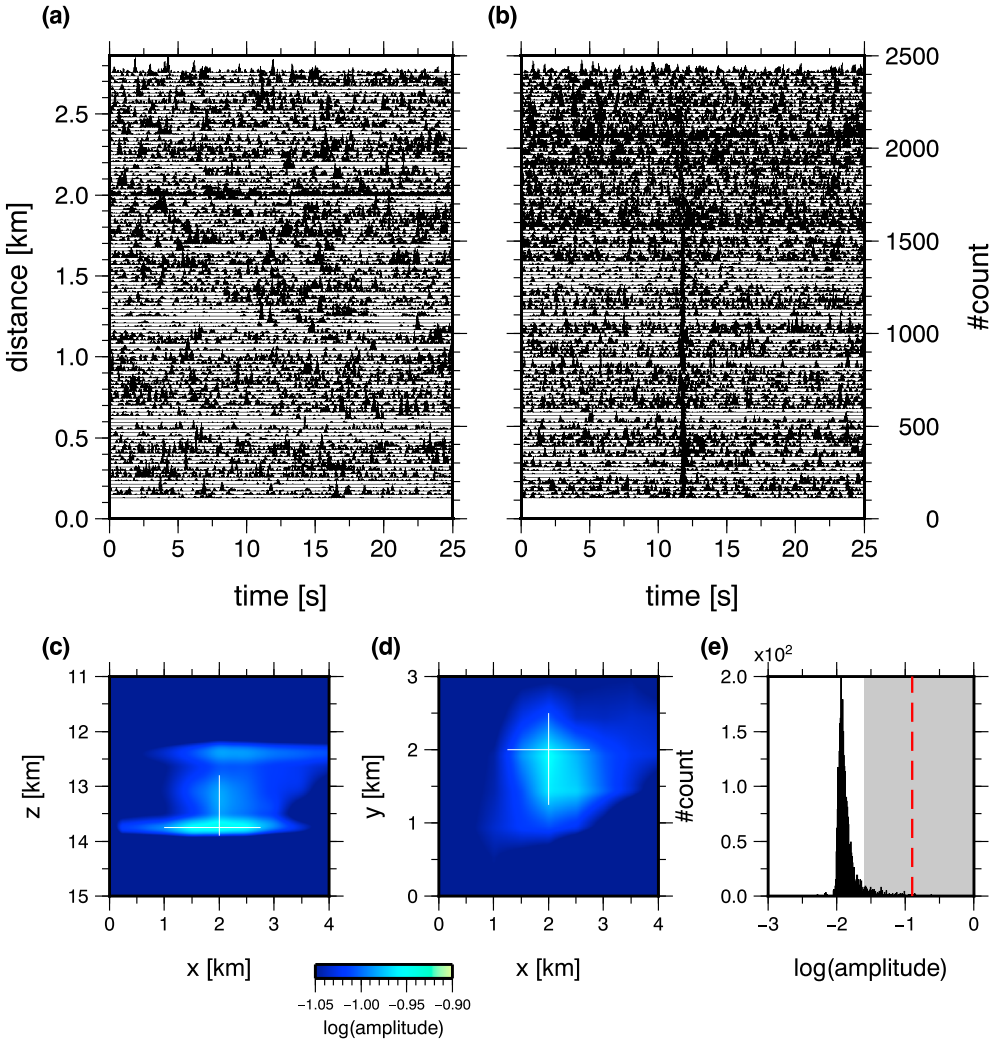

Figure 2. Amplitude as a function of time for traces containing a $M_w = 0.4$ and back-projected stack amplitude as a function of position. (a) Waveform envelopes before downward continuation. (b) After downward continuation to a depth of 5 km. Vertical axes indicate epicentral distance (left) and trace count (right). Traces are normalized by their maximum. (c) Log of maximum stack power for a 5 s window projected onto a vertical cross-section oriented EW. (d) Map view of log of maximum stack power averaged over a depth range between 10 and 16 km. 1-MAD location uncertainty is indicated by white lines. (e) Histogram of log of stack maxima in a 4 h window around the detected event. Grey rectangle indicates region of acceptance, and red dashed curve indicates log of the stack maxima for the $M_w = 0.4$ event.

exponential distributions (Figures 2e and 4c). Thus, the likelihood of false detections may be estimated from the ratio of the noise and signal's cumulative probabilities. We define a detection threshold equal to 5 times the median absolute deviation (MAD) of the noise distribution, which corresponds to 3.4 sigma above the mean of the distribution. To estimate the probability of exceeding this threshold, we generate 1000 realizations of Gaussian noise whose variance is equal to the variance of the backprojection images. We select the maxima in each realization and use a maximum-likelihood estimator to obtain the best fitting Gumbel distribution parameters. The probabilities that a variable drawn from a Gumbel distribution will exceed the 5-MAD and 2-MAD thresholds are 3.22×10^{-7} and 1.27×10^{-4}, which translates to a constant rate of about 2×10^{-3} and one false alarm per night. The location uncertainties are estimated from the 1-MAD intervals around the maxima of the backprojection image and are about 5 and 1 km in the vertical and horizontal directions for the deepest events in our catalog but less than that for events occurring above 15 km (Figure 2). More details on event detection are presented in the supporting information.

Our approach does not take into account any lateral heterogeneities in the velocity field, which may differ significantly from theoretical traveltimes computed using a 1-D model. Thus, a detailed 3-D velocity model should improve the accuracy of hypocentral locations. However, for the expected range of source-receiver distances in LB, the available 3-D model would only slightly modify the computed traveltimes and hence introduce slight shifts to the locations obtained with a 1-D model. To confirm that, we compared traveltime predictions from the CVM-H velocity model to the predicted traveltimes using the 1-D model and found that the residuals are up to 5% of the traveltime along the path, which would introduce location shifts that are smaller than our location uncertainties. This suggests that our interpretations are not strongly dependent on the velocity model we use.

In order to determine the magnitude of the detected events we use a simulation-based calibration scheme. Unfortunately, the Southern California Seismic Network (SCSN) catalog does not contain any events that occurred during the survey within the target volume, which forces us to use a model to calibrate the amplitudes. We compute the surface seismograms due to a strike-slip point source with $M_w = 1$ and a 3 MPa stress drop using the frequency-wave number wave propagation method of *Zhu and Rivera* [2002] together with the CVM-H velocity and *Hauksson and Shearer's* [2006] attenuation models. The entire catalog is calibrated with a single event since the corner frequencies of the reference and recorded events are much higher than the frequencies we analyze. In the same fashion as the real data, the synthetics are normalized, downward continued, back projected onto the input hypocentral locations, which populate the target volume at 1 and 2 km spacing in the horizontal and vertical directions, and interpolated to a finer grid using bicubic interpolation. Since the raw data are normalized by their hourly RMS, the process is repeated for the synthetic data using the RMS values of the raw traces. Our procedure determines event magnitudes from the amplitude ratio between the observed and synthetic data. Because the synthetic data are produced with a realistic attenuation model, the procedure does not require that we apply any attenuation corrections.

3. Active Faults Beneath Long Beach

Downward continuation and backprojection of the LB data reveal numerous events occurring beneath the array. Our detection procedure brings these signals well above the background noise level (Figure 2) and allows us to obtain a high-resolution image of active faults in LB. Figure 3 presents the density of detections. Surprisingly, the events are mostly located to the south of the mapped trace of the NIFZ, where clustered seismicity delineates structures dipping to the southwest and the northeast (Figure 3c). These are a common feature in tectonic environments such as the LA basin, in which the regional stress field transitioned from extension to compression, and may indicate reactivation of steeply dipping faults inside the basin [*Williams et al.*, 1989]. Event depths gradually increase to the northeast of the NIFZ (Figure 3c). This result is consistent with a gently dipping detachment fault that has been previously proposed to cut beneath the NIFZ [*Davis et al.*, 1989; *Shaw and Suppe*, 1996], but it is not well resolved with the distribution of earthquakes shown in Figure 3 due to the scarcity of events north of the NIFZ.

While seismicity in the upper 15 km may be associated with faults that extend beneath LB, deeper events occur almost uniformly within the studied volume. The event depths and the corresponding uncertainties confirm that a considerable fraction of the seismicity in the area occurs in the lower crust or perhaps even in the mantle. We compare our focal depth distribution to the distribution in the SCSN catalog in Figure 3e. The two catalogs generally agree down to depths of about 15 km but differ significantly below that. This is likely due to the fact that the size distribution of events at greater depths is dominated by earthquakes with $M_w < 1$, about one unit smaller than the SCSN catalog magnitude of completeness for LB (Figure 4a) and are therefore missing in the SCSN catalog.

Oil production in LB has been known to induce seismic and aseismic deformation. Between 1937 and 1967 a region located above the Wilmington Oil Filed experienced rapid subsidence that reached as much as 9 m at several locations and was accompanied by several shallow M2.4–3 events. Those events are thought to be the result of fluid extraction in the Wilmington Oil Field [*Kovach*, 1974; *Segall*, 1989]. Since 1953, removal of fluids in the Wilmington Oil Field and LB Oil Field is compensated by water injection. The epicentral distribution in Figure 3 suggests that oil field activities have a negligible effect on the microseismicity below 5 km [*Hauksson et al.*, 2015]. Due to downward continuation, events with $M < 1$ occurring in the uppermost 5 km are likely to be missed from our catalog. Visual inspection of SCSN records of shallow M1 events in LB suggests that this is

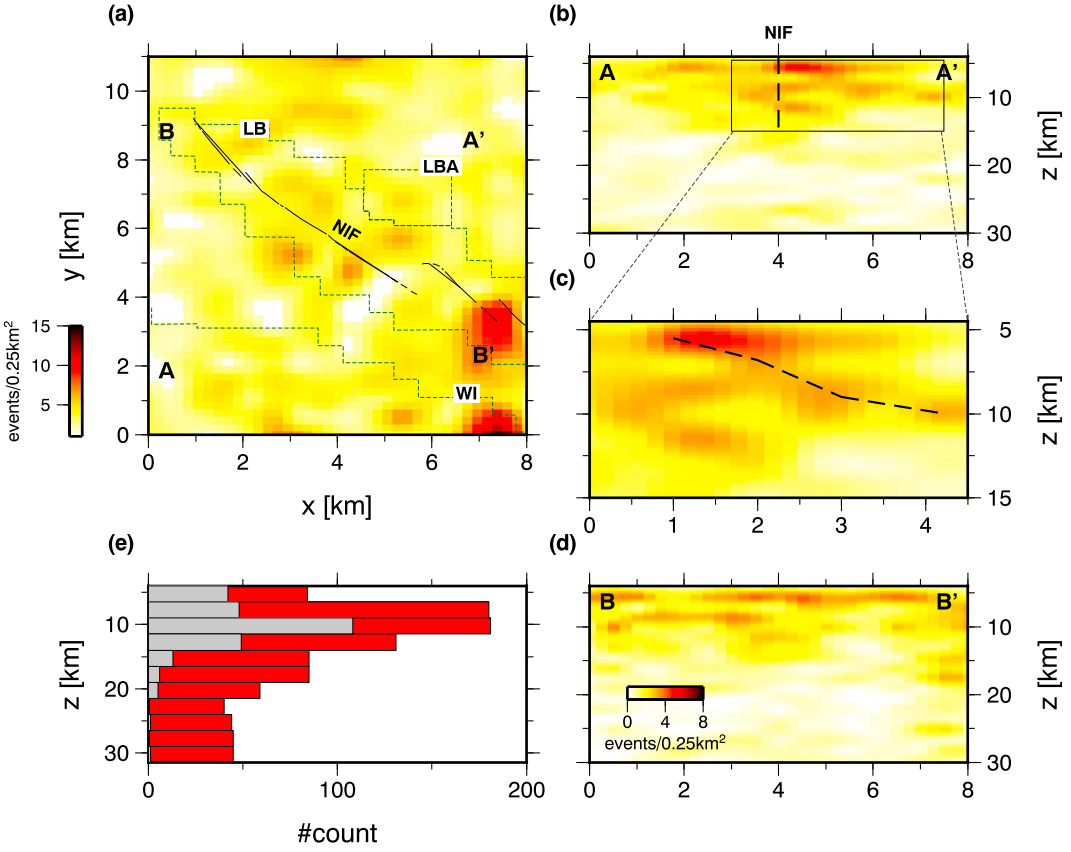

Figure 3. Earthquake location density. (a) Events density as a function of position. Black and dashed green lines are for faults and oil fields, respectively. In Figures 3b–3d density of hypocenters projected onto vertical planes whose surface traces are indicated by letters in Figure 3a, with Figure 3c containing the distribution within an area indicated by a rectangle in Figure 3b. Note the difference in color scales between map and cross sections. (e) Event count as a function of hypocental depth for the back-projection (red) and the relocated catalog of *Hauksson et al.* [2012] (grey). NIF: Newport-Inglewood Fault. B: Long Beach Oil Field, LBA: Long Beach Airport Oil Field, WI: Wilmington Oil Field.

approximately the magnitude cutoff for SCSN detection in LB. This could be considerably improved by using the LB data set with a technique that is focused on the upper 5 km.

3.1. Event Size Distribution and Seismicity Rate

To confirm that the event population consists primarily of tectonic events we analyze the spatiotemporal distribution of microseismicity in the newly compiled catalog. Next, we show that attributes common to earthquake populations in most other tectonic environments are also present in the backprojection catalog.

Earthquake populations obey two well-known empirical relations, the Gutenberg-Richter frequency-magnitude distribution and the modified Omori's law [*Utsu*, 1961]. The first relation states that N, the number of events whose magnitude is larger than some magnitude M, is a logarithmic function of magnitude such that:

$$\log_{10} N = a - bM, \tag{4}$$

where the parameter a describes the total number of earthquakes and the parameter b, commonly referred to as the b-value, describes the ratio between large and small earthquakes. In different tectonic environments earthquake size distributions are well fitted by a Gutenberg-Richter relation with a b value that lies between 0.8 and 1.2. Figures 4a and 4b present the number of detected events as a function of their magnitude for two depth ranges. For comparison, we also plot the frequencies in a catalog compiled with a detection threshold equal to twice the MAD of the logarithm of the maximum stack power. We find that the detected earthquakes size distribution obeys the Gutenberg-Richter relation with a b value approximately equal to one at depths

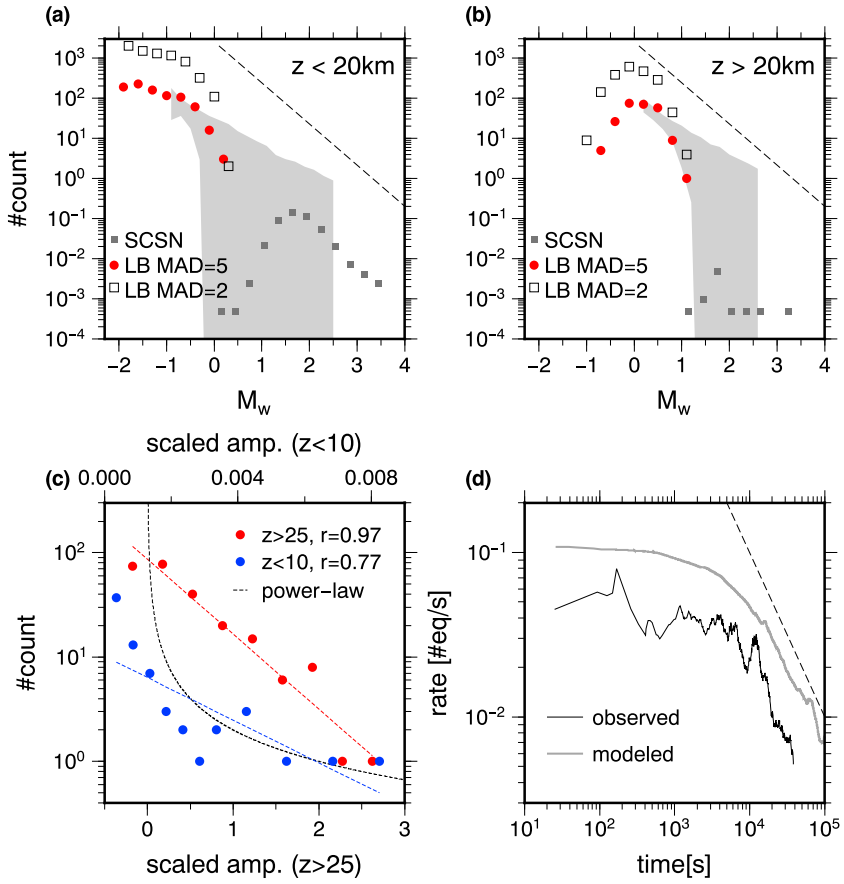

Figure 4. Earthquake size distribution and productivity. (a–b) Earthquake count as a function of magnitude. In Figures 4a and 4b are for events whose depth is above and below 20 km, respectively. Red circles and white squares are for the LB backprojection catalog with MAD> 2 and MAD> 5 detection threshold, respectively, and grey squares are for the SCSN catalog. Slope of dashed reference curves is equal to −1. Grey area indicates the expected variability in frequency distributions from synthetic catalogs with a *b* value that lies between 0.9 and 1.1. (c) Earthquake count as a function of amplitude scaled by the amplitude of a synthetic source. Red and blue circles are for events occurring below 25 km and above 10 km, respectively. Red and blue dashed curves indicate the best-fitting linear model and their correlation coefficients. Dashed black curve is for a power law with an exponent equal to 1. (d) Rate of earthquakes with $M_w > 0$ as a function of time since main shocks derived from a composite catalog. Black and grey curves are for observed and modeled seismicity rates, with the latter offset vertically for clarity. Dashed curve indicates the $1/t$ Omori-like decay.

shallower than 20 km but deviates from this relation at larger depths. This is illustrated in Figure 4c, which shows the distribution of recorded amplitudes scaled by the amplitude of a reference event with $M_w = 1$ for depth ranges below 15 and above 25 km. When plotted on a semilog scale, the amplitude distribution of the deeper events is well fitted by a linear model (i.e., exponential distribution), while the shallower events amplitude distribution is not. As a test on the consistency of our magnitude scale, we also plot the event size distribution from the SCSN catalog between 1970 and 2013 for a region that is twice as large as the area of the array and normalize the frequencies by a factor that is equal to one half the ratio of the time interval covered by our catalog to the one covered in the SCSN catalog. That the size distribution in our catalog is consistent with the frequencies of larger events found in the SCSN catalog confirms that our magnitude estimation is robust.

The quality of the earthquake catalog may be estimated from its magnitude of completeness, defined as the magnitude below which the frequency-magnitude distribution deviates from the Gutenberg-Richter power law and which depends mostly on station density and SNR conditions. While the SCSN station density is the highest in the LA basin, the SNR is low there due to urban noise, resulting in poorer detection capabilities than along other faults in southern California. Our newly compiled catalog for LB is complete down to

$M_w \approx -0.5$ and $M_w \approx 0$ above and below 20 km, (Figures 4a and 4b), and that the completeness is only modestly dependant on the detection threshold we apply (Figures 4a and 4b).

Our results represent a significant improvement over the detection capability of the SCSN catalog, which is only complete down to $M_w \approx 2$. Since the frequency-magnitude distribution above 20 km obeys a power law with exponent near 1, the improvement of over 2 orders of magnitude in catalog completeness yields a hundred-fold decrease in the time needed for effective seismic monitoring in LB.

Figures 4a, 4b, and 4c suggest that with increasing depth the frequency-magnitude distribution decays exponentially. This is reminiscent of the transition as a function of depth in faults with nonvolcanic tremors from shallow seismicity with regular Gutenberg-Richter behavior to deep low-frequency earthquakes with exponential amplitude distribution [*Watanabe et al.*, 2007] or to the observed increase in b value near the geodetically inferred locking depth in California [*Spada et al.*, 2013]. In earthquake models involving populations of frictionally unstable asperities embedded in stably sliding areas [*Dublanchet et al.*, 2013a, 2013b], a narrower frequency-magnitude distribution can be explained by a weaker interaction between asperities due to a lower density of asperities or to a higher resistance of the creeping region. The latter is consistent with the increase of velocity strengthening with temperature in laboratory friction experiments. Figure 3 suggests that events occurring at depth shallower than 15 km are more clustered than deeper events. Thus, the bulk majority of deep earthquakes seem to occur almost uniformly within the studied volume, which is an indication that seismicity becomes more diffused with increasing depth. This observation is consistent with the hypothesis that it is the decrease of asperity density that is responsible of the rapid falloff in the magnitude of deep events beneath LB.

Temporal clustering of aftershocks is well described by the modified Omori's law, which states that seismicity rate, $\dot{N}$, decays with time since the main shock as

$$\dot{N} = \frac{K}{(t+c)^p}, \tag{5}$$

where K and c are fitting coefficients and the value of p is usually close to one. Traditionally, only large and infrequent earthquakes are treated as main shocks. However, several studies show that similar to large main shocks, small earthquakes trigger their own aftershock sequences, which decay according to the modified Omori's law [*Helmstetter et al.*, 2005; *Marsan*, 2005; *Ziv*, 2006b; *Marsan and Lengliné*, 2008].

When analyzing aftershocks of microearthquakes, it is instructive to compile a composite catalog by stacking many main shock-aftershock pairs. This approach assumes that each event is a potential main shock in a sense that it can trigger its own aftershock sequence. To reduce the bias due to the incompleteness of the catalog, we only use events with $M_w > 0$. To compile a composite catalog, we first compute lag times and distances between each potential main shock and all successive events and then stack main shock-aftershock pairs according to their interevent distances in 1 km distance bins. Using a smaller range results in too few events for robust rate estimation, while a larger range may obscure the rate changes because remote sites experience negligible stress change at short lag times following the main shock. We follow *Ziv et al.* [2003] and compute the seismicity rate by using a sliding data window. We compute the rate for an initial window containing five earthquakes, slide the window by one event and increase the window size by two events. The last step is repeated until a predefined size is reached, after which the window size is constant. Figure 4d presents the seismicity rate as a function of time for stacked aftershock sequences that occur within 1 km from the potential main shocks. Figure 4d also shows the seismicity rate in a synthetic composite catalog generated from a statistical model of aftershock occurrence [e.g., *Felzer and Kilb*, 2009], in which the values of b, p, and c are equal to 1, 1.2, and 6000 s, respectively. Since the catalog is complete for lag times larger than 10 s, we interpret the flat early rate as a true feature of the seismicity, in accordance with predictions of a physical model of aftershock occurrence [*Dieterich*, 1994], and observations from other well-studied faults in California [*Ziv et al.*, 2003; *Rubin*, 2002]. The supporting information contains the results from synthetic tests which demonstrate that this behavior is not reproduced in catalogs with uncorrelated background activity. We find that the observed and modeled rates are in good agreement and conclude that the seismicity rates decay according to the modified Omori's law with a p value that is approximately one.

4. Conclusions

Analysis of data from the dense LB array reveals numerous, previously undetected microearthquakes. The detection is made possible by first downward continuing the recorded wavefield. The new catalog magnitude of completeness for events occurring above 20 km is $M_w \approx -0.5$, more than two magnitude units less than the SCSN catalog magnitude of completeness in LB for this depth range. Several clusters occur on faults to the north and south of the mapped trace of the NIFZ. Many hypocenters are located at depths larger than 20 km. Evidence of a thin crust beneath the study area and the estimated location uncertainty imply that many of the events occur in the mantle. The seismic activity at depths larger than 5 km is uncorrelated with oil extraction in the LB Oil Field and Wilmington Oil Field or the mapped trace of the NIFZ.

Earthquake size distribution in LB follows a power law with a *b* value that is approximately equal to one for events that occur in the range of 5–20 km and is exponentially distributed at larger depths. The backprojection catalog exhibits strong temporal clustering dominated by aftershock sequences. Temporal analysis of a composite catalog shows that aftershock rate decays according to the modified Omori's law, with a *p* value that is approximately one.

Acknowledgments

We thank Dan Hollis of Nodalseismic Inc for supplying the data used in this study and Signal Hill Petroleum for giving permission to use it. Comments from two anonymous reviewers have helped improve this manuscript. This work was supported by the NSF award EAR-1214912 and a THOR award that funded the mass-storage system for data archiving.

The Editor thanks two anonymous reviewers for their assistance in evaluating this paper.

References

Barrows, A. G. (1974), A review of the geology and earthquake history of the Newport-Inglewood structural zone, southern California, *Calif. Div. Mines Geol. Spec. Rep. 114*, Calif. Dep. of Conserv., Div. of Mines and Geol., Sacramento, Calif.

Bouchon, M., H. Karabulut, M. Aktar, S. Ozalaybey, J. Schmittbuhl, and M.-P. Bouin (2011), Extended nucleation of the 1999 M-w 7.6 Izmit earthquake, *Science*, *331*(6019), 877–880, doi:10.1126/science.1197341.

Bouchon, M., V. Durand, D. Marsan, H. Karabulut, and J. Schmittbuhl (2013), The long precursory phase of most large interplate earthquakes, *Nat. Geosci.*, *6*(4), 299–302, doi:10.1038/NGEO1770.

Bryant, A. G. (1988), Recently active traces of the Newport-Inglewood fault zone, Los Angeles and Orange Counties, *Calif. Div. Mines Geol. Open File Rep., 88–14*, Calif. Dep. of Conserv., Div. of Mines and Geol., Sacramento, Calif.

Claerbout, J. F. (1976), *Fundamentals of Geophysical Data Processing: With Applications to Petroleum Prospecting*, McGraw-Hill, New York.

Davis, T. L., J. Namson, and R. F. Yerkes (1989), A cross section of the Los Angeles Area: Seismically active fold and thrust belt, The 1987 Whittier Narrows earthquake, and earthquake hazard, *J. Geophys. Res.*, *94*(B7), 9644–9664, doi:10.1029/JB094iB07p09644.

Dieterich, J. (1994), A constitutive law for rate of earthquake production and its application to earthquake clustering, *J. Geophys. Res.*, *99*(B2), 2601–2618, doi:10.1029/93JB02581.

Dublanchet, P., P. Bernard, and P. Favreau (2013a), Creep modulation of Omori law generated by a Coulomb stress perturbation in a 3-D rate-and-state asperity model, *J. Geophys. Res. Solid Earth*, *118*, 4774–4793, doi:10.1002/jgrb.50311.

Dublanchet, P., P. Bernard, and P. Favreau (2013b), Interactions and triggering in a 3-D rate-and-state asperity model, *J. Geophys. Res. Solid Earth*, *118*, 2225–2245, doi:10.1002/jgrb.50187.

Felzer, K. R., and D. Kilb (2009), A case study of two M ~5 m mainshocks in Anza, California: Is the footprint of an aftershock sequence larger than we think?, *Bull. Seismol. Soc. Am.*, *99*(5), 2721–2735, doi:10.1785/0120080268.

Gazdag, J. (1978), Wave-equation migration with phase-shift method, *Geophysics*, *43*(7), 1342–1351, doi:10.1190/1.1440899.

Hauksson, E., and S. Gross (1991), Source parameters of the 1933 Long-Beach earthquake, *Bull. Seismol. Soc. Am.*, *81*(1), 81–98.

Hauksson, E., and P. M. Shearer (2006), Attenuation models (Qp and Qs) in three dimensions of the southern California crust: Inferred fluid saturation at seismogenic depths, *J. Geophys. Res.*, *111*, B05302, doi:10.1029/2005JB003947.

Hauksson, E., T. Göbel, J.-P. Ampuero, and E. Cochran (2015), A century of oil-field operations and earthquakes in the greater Los Angeles Basin, southern California, *Leading Edge*, *34*(6), 650–656, doi:10.1190/tle34060650.1.

Hauksson, E., W. Yang, and P. M. Shearer (2012), Waveform relocated earthquake catalog for Southern California (1981 to June 2011), *Bull. Seismol. Soc. Am.*, *102*(5), 2239–2244, doi:10.1785/0120120010.

Helmstetter, A., Y. Y. Kagan, and D. D. Jackson (2005), Importance of small earthquakes for stress transfers and earthquake triggering, *J. Geophys. Res.*, *110*, B05S08, doi:10.1029/2004JB003286.

Kovach, R. L. (1974), Source mechanisms for Wilmington Oil Field, California, subsidence earthquakes, *Bull. Seismol. Soc. Am.*, *64*(3), 699–711.

Lin, F.-C., D. Li, R. W. Clayton, and D. Hollis (2013), High-resolution 3D shallow crustal structure in Long Beach, California: Application of ambient noise tomography on a dense seismic array, *Geophysics*, *78*(4), Q45–Q56, doi:10.1190/GEO2012-0453.1.

Marsan, D. (2005), The role of small earthquakes in redistributing crustal elastic stress, *Geophys. J. Int.*, *163*(1), 141–151, doi:10.1111/j.1365-246X.2005.02700.x.

Marsan, D., and O. Lengliné (2008), Extending earthquakes' reach through cascading, *Science*, *319*(5866), 1076–1079, doi:10.1126/science.1148783.

Plesch, A., C. Tape, J. R. Graves, P. Small, G. Ely, and J. H. Shaw (2011), Updates for the CVM-H including new representations of the offshore Santa Maria and San Bernardino basin and a new Moho surface, paper presented at Southern California Earthquake Center Annual Meeting, Palm Springs, Calif.

Rubin, A. M. (2002), Aftershocks of microearthquakes as probes of the mechanics of rupture, *J. Geophys. Res.*, *107*(B7), 2142, doi:10.1029/2001JB000496.

Rubin, A. M., D. Gillard, and J. L. Got (1999), Streaks of microearthquakes along creeping faults, *Nature*, *400*(6745), 635–641, doi:10.1038/23196.

Segall, P. (1989), Earthquakes triggered by fluid extraction, *Geology*, *17*(10), 942–946, doi:10.1130/0091-7613(1989)017<0942:ETBFE>2.3.CO;2.

Shaw, J. H., and J. Suppe (1996), Earthquake hazards of active blind-thrust faults under the central Los Angeles basin California, *J. Geophys. Res.*, *101*(B4), 8623–8642, doi:10.1029/95JB03453.

Spada, M., T. Tormann, S. Wiemer, and B. Enescu (2013), Generic dependence of the frequency-size distribution of earthquakes on depth and its relation to the strength profile of the crust, *Geophys. Res. Lett.*, *40*, 709–714, doi:10.1029/2012GL054198.

Süss, M. P., and J. H. Shaw (2003), P wave seismic velocity structure derived from sonic logs and industry reflection data in the Los Angeles basin, California, *J. Geophys. Res.*, *108*(B3), 2170, doi:10.1029/2001JB001628.

U.S. Geological Survey (2015), *Quaternary Fault and Fold Database for the United States*, U.S. Geol. Surv., Reston, Va.
Utsu, T. (1961), A statistical study on the occurrence of aftershocks, *Geophys. Mag.*, *30*, 521–605.
Watanabe, T., Y. Hiramatsu, and K. Obara (2007), Scaling relationship between the duration and the amplitude of non-volcanic deep low-frequency tremors, *Geophys. Res. Lett.*, *34*, L07305, doi:10.1029/2007GL029391.
Williams, G. D., C. M. Powell, and M. A. Cooper (1989), Geometry and kinematics of inversion tectonics, *Geol. Soc. London Spec. Publ.*, *44*(1), 3–15, doi:10.1144/GSL.SP.1989.044.01.02.
Wright, T. L. (1991), Structural geology and tectonic evolution of Los-Angeles basin, *AAPG Bull.*, *71*(5), 629.
Yang, W., E. Hauksson, and P. M. Shearer (2012), Computing a large refined catalog of focal mechanisms for Southern California (1981-2010): Temporal stability of the style of faulting, *Bull. Seismol. Soc. Am.*, *102*(3), 1179–1194, doi:10.1785/0120110311.
Zhu, L. P., and L. A. Rivera (2002), A note on the dynamic and static displacements from a point source in multilayered media, *Geophys. J. Int.*, *148*(3), 619–627, doi:10.1046/j.1365-246X.2002.01610.x.
Ziv, A. (2006a), On the role of multiple interactions in remote aftershock triggering: The Landers and the Hector Mine case studies, *Bull. Seismol. Soc. Am.*, *96*(1), 80–89, doi:10.1785/0120050029.
Ziv, A. (2006b), Does aftershock duration scale with mainshock size?, *Geophys. Res. Lett.*, *33*, L17317, doi:10.1029/2006GL027141.
Ziv, A., A. M. Rubin, and D. Kilb (2003), Spatiotemporal analyses of earthquake productivity and size distribution: Observations and simulations, *Bull. Seismol. Soc. Am.*, *93*(5), 2069–2081, doi:10.1785/0120020117.